



HAL
open science

Front End Electronics for Radiation Detectors Based on SiC: Application to High Dose per Pulse Charged Particle Beam Current Measurement

A. Tchoualack Tchamako, Laurent Ottaviani, Wenceslas Rahajandraibe, Wilfried Vervisch, Vanessa Vervisch, Jean-Pierre Walder

► **To cite this version:**

A. Tchoualack Tchamako, Laurent Ottaviani, Wenceslas Rahajandraibe, Wilfried Vervisch, Vanessa Vervisch, et al.. Front End Electronics for Radiation Detectors Based on SiC: Application to High Dose per Pulse Charged Particle Beam Current Measurement. IEEE Sensors Journal, 2022, 22 (3), pp.2326-2337. 10.1109/JSEN.2021.3117864 . hal-04026007

HAL Id: hal-04026007

<https://hal.science/hal-04026007v1>

Submitted on 13 Mar 2023

HAL is a multi-disciplinary open access archive for the deposit and dissemination of scientific research documents, whether they are published or not. The documents may come from teaching and research institutions in France or abroad, or from public or private research centers.

L'archive ouverte pluridisciplinaire **HAL**, est destinée au dépôt et à la diffusion de documents scientifiques de niveau recherche, publiés ou non, émanant des établissements d'enseignement et de recherche français ou étrangers, des laboratoires publics ou privés.

Front End Electronic for Radiation Detectors Based on SiC: Application to High Dose per Pulse Charged Particle Beam Current Measurement

A Tchoulack, L.Ottaviani, W.Rahajandraibe, W.Vervisch, V.vervisch J.P.Walder
Aix Marseille University,CNRS, University of Toulon, IM2NP UMR 7334, Marseille, France

Abstract—In high dose per pulse charged particle beams, all online detectors saturate due to ion recombination. It is therefore impossible to count detector pulses separately. Silicon carbide due to its high band gap, high thermal conductivity and high displacement energy, is seen as an alternative. Analyzing waveforms in real time is challenging in terms of bandwidth, measurable energy range, sensor size, data rate. In this context, an Analog Front-End (AFE) was designed for radiation signal processing. It is based on a TransImpedance Amplifier (TIA) and Charge Sensitive Amplifier (CSA) to analyze the shape of generated signal. The methodology used to characterize AFE for high detector capacitance is described. The results extracted from simulations, experimental and measurements in radiative environment are also presented.

Index Terms—Charged particle, Dose per Pulse, SiC, TIA, CSA, Stability, Linac.

I. INTRODUCTION

Nowadays, Silicon Carbide (SiC) is among the semiconductors used as sensors in radiation detection [1], [2]. The various researches on the silicon carbide pixilation thanks to the reduction and the integration capacity of the reading electronics has allowed to improve its competitive position compared to photomultipliers, ionization chambers and film dosimetry. On the other hand, its carbonaceous nature ($Z = 6$) makes it a good "tissue equivalent" and it has a very short response time thank to its high carrier saturation velocity [3]. Today, in harsh environment applications, the sensors suffer from fragility at high dose of irradiation owing to their low thermal conductivity, breakdown electrical fields and threshold displacement energy [4], [5]. In semiconductor, charged particle lose its energy by creating a pairs of electrons holes [6], [7], [8]. After being generated by the sensor, the signal must be conditioned. Most of the existing conditioning [9] chains are based on CSA (charge sensitive amplifier) or PAI (current preamplifier) in order to detect current created by the crossing of an ionizing particle through the sensor (Fig.1). In this context current preamplifier and charge sensitive amplifier have been studied [10], [11]. First of all when the particle flow becomes sufficiently high in terms of flux and energy (up to $10^7 \text{ n.cm}^{-2}.\text{s}^{-1}$), the current generated by the sensor is composed in two parts: one continuous part and another part with variations around this continuous value. With such

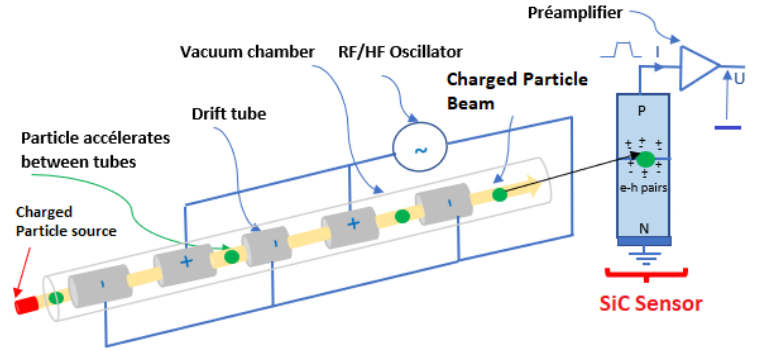


Fig. 1. Schematic diagram showing a particle extracted from an charged particle source then accelerated through a Linac (Linear Accelerator) and which subsequently interacts with a Silicon Carbide Detector. The generated signal is then conditioned using a preamplifier (PAI/CSA).

pulse, a reading amplifier with a fast response and fast fall time ($\text{tr} < 150\text{ns}$ and $\text{tf} < 150\text{ns}$) time is required. Then PAI should be used. On the other hand, when the particle flow is not high in terms of flux and energy ($\phi < 10^6 \text{ n.cm}^{-2}.\text{s}^{-1}$), the current generated by the sensor has low value in terms of amplitude and time ($\approx \text{nA}$ and $\approx \text{ns}$ respectively) [12]. Then CSA should be used.

The aim of this work is to study SiC based radiation detector response thanks to AFE. For that, the paper is organized as follows. Section II presents the used methodology, and section III, the system study. In section IV we will present material, test method and measurement results. Section V is devoted to discussion and conclusion.

II. METHODOLOGY

The readout electronic diagram used is presented in Fig.2. In this work we focused on SiC sensor and analog Amplifier. This bloc consist on two operating modes. In TIA mode, the output presents derivatives of the output signal due to the presence of the detector capacitance [13]. Its derivatives can be attenuated by feedback capacitance thus allowing to move the poles of the transfer function. Then process of recovering the waveform of the signal coming from the detector will be in a frequency range (zero phase) for input impedance. In the case of CSA (Charge Sensitive Amplifier) structure, the charge

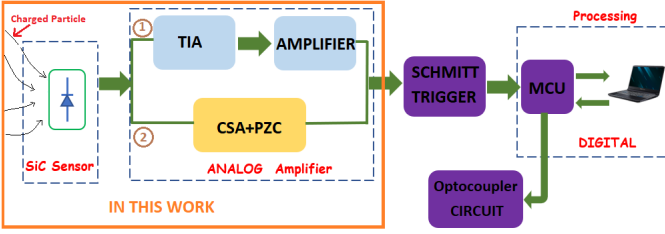


Fig. 2. Readout electronics for particle detection. TIA or CSA are used to read charged particle beam. Pulse counting is carried out using MCU. When setpoint have reached, the computer send a signal to the optocoupler circuit to stop Linac.

Property	Si	GaN	Diamond	4H-SiC
Bandgap (eV)	1.12	3.45	5.5	3.27
Break down field (MV cm ⁻¹)	0.3	2	10	3
e-hole creation energy (eV)	3.6	8.9	13	7.78
Threshold displacement energy (eV)	13-20	10-20	40-50	22-35
Thermal conductivity (W/cm K)	1.5	1.3	22	4.9

TABLE I
SEMICONDUCTOR MATERIAL USED IN RADIATION DOMAIN.

collection process can be incomplete due to the reduced value of OP-Amp DC gain and also the bandwidth of this one. In other word, these limitations will have the effect of attenuating the electronic output signal. The PAI/CSA structures are built around a low noise amplifier, accepting the input signal in form of a current/charge from a high impedance signal source, as a photodiode or a semiconductor based detector for radiation particles [14]. This amplifier converts signal into an output voltage. Generally, this structure is not advisable if the sensor device has a large capacitance (>200pF), and if fast rise time is required [15].

III. SYSTEM STUDY

A. Silicon Carbide Material (SiC)

Harsh environment applications require thermal and physical stability of sensor parameters. Thus, both intrinsic properties of the semiconductor and the device architecture play a critical role for stability. In semiconductor materials, harsh environment leads to a decrease in the energy band gap and an increase in carrier concentration, which in turn adversely affects the sensor performance [16]. Materials with high bandgap and low intrinsic carrier concentration are needed for harsh environment applications see Tab.I. SiC possesses a higher energy bandgap compared to the more widely used Si and GaAs materials.

The comparative evolution of intrinsic carrier concentration of Si and SiC with temperature is presented in Fig.3. For operation in semiconductor device, the intrinsic carrier density should be well below the intentional dopant induced carrier density [17]. For instance, the intrinsic carrier density of Si is 10^{10} cm^{-3} and well below the typical dopant induced carrier densities. For 4H-SiC, the intrinsic carrier density is 10^{-10} cm^{-3} . The correlation of intrinsic concentration (ni) and temperature is given by:

$$n_i = [N_c \cdot N_v]^{1/2} \cdot \exp\left[-\frac{E_g(T)}{2KT}\right] \quad (1)$$

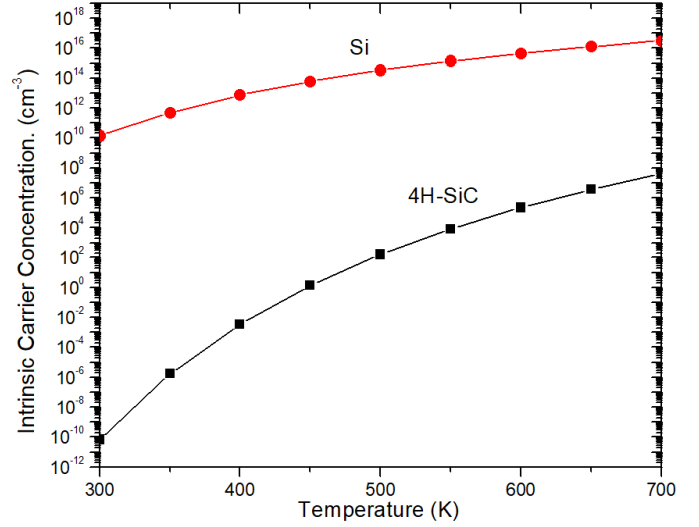


Fig. 3. Intrinsic carrier concentration of Si is 10^{10} cm^{-3} well below the typical dopant-induced carrier densities. For 4H-SiC, the intrinsic carrier density is 10^{-10} cm^{-3} at 300K.

Semiconductor	Si	GaAs	4H-SiC
Breakdown voltage (V) for doping concentration N_d	$2.96 \times 10^{17}/N_d$	$5.76 \times 10^{17}/N_d$	$249 \times 10^{17}/N_d$
Drift region width (cm) for breakdown voltage V_B	$6.67 \times 10^{-6} V_B$	$5.00 \times 10^{-6} V_B$	$0.67 \times 10^{-6} V_B$

TABLE II
SEMICONDUCTOR PARAMETER.

As shown in Fig.3, the intrinsic carrier concentration of SiC stays well below allowable limits even at 700K, allowing operation of SiC sensor at extremely harsh environment without suffering from intrinsic conduction effects and presenting low dark current. Drift region widths and breakdown voltages of Si, GaAs, 4H-SiC, and 6H-SiC are shown in TABLE II.

B. SiC Neutron detector

Neutrons are classified into three categories: Thermal, Epithermal and Fast neutrons as indicated Fig.4 [18].

Neutron is neutral particle. Thermal neutron ($E=0.025\text{eV}$) detection is based on indirect methods (see Fig.5 and Fig.6

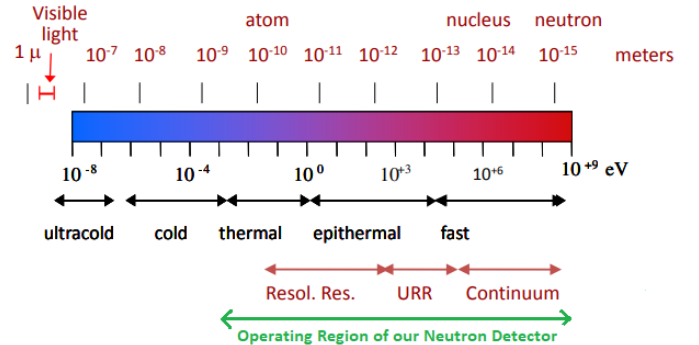


Fig. 4. Spectrum of neutron energy from ultracold neutrons to fast neutrons. The wavelength of the neutrons; the de Broglie wavelength; is also shown and compared with dimensions of visible light waves and atomic, nuclear, and nucleon dimensions.

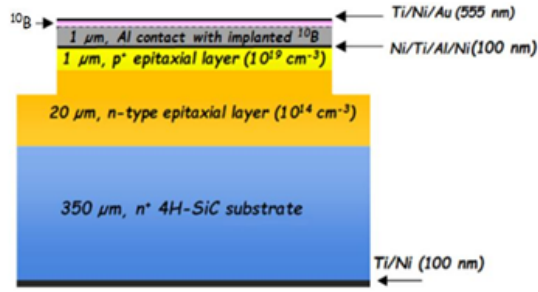
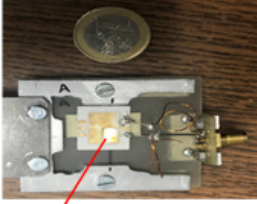


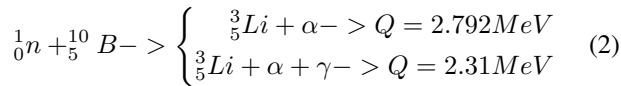
Fig. 5. Silicon Carbide detector configuration with ^{10}B as neutron converter layer for neutron conversion into charged particles (see [8]).



SiC detector Capacitance (p)	Optimal bias voltage(V)	Sensor's area (mm ²)	Active layer thickness (μm)
270	-200	33	20

Fig. 6. SiC sensor parameter and his houser.

for sensor parameters)[19]. Thermal neutrons interact with Neutron Converter Layer (NCL) containing (boron isotope 10) resulting in the production of alpha particle and lithium according to the following reactions [20].



Interaction of these charged particles with the detector's sensitive volume produces free charge carriers. The primary function of this detector is to detect neutrons which can be two types: thermal or fast ($E_n=0.025\text{eV}$ or $E_n>10\text{MeV}$ respectively). This detector as part of our tests was used for neutron detection [21]. The PAI/CSA used in large numbers of front-end for radiation detector is a key block [22], since it sets the limits to the performance of the whole system and it must satisfy conflicting requirements such as low noise, low power, and wideband operation. The following sections are devoted to TIA and CSA analysis. All the electrical results presented in this work were done without detector polarization.

C. Transimpedance function

The detector current pulse is transformed into voltage help to Transimpedance Amplifier (TIA) depicted in Fig.7 [23]. It presents derivatives of the output signal due to the presence of the detector capacitance. The amplifier's must be stabilized by a suitably chosen feedback capacitance C_f . Owing to the presence of these capacitance (C_f), and because of the

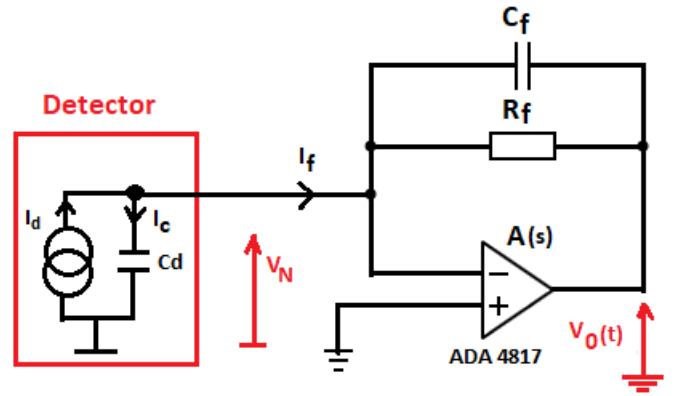


Fig. 7. Transimpedance built around an high speed and low noise amplifier.

amplifier's own limitations, the system response at high frequencies will be reduced and then decrease the rising time [24].

1) *Transimpedance analysis:* Amplifier's (OA) voltage gain is modeled in Laplace space as:

$$A(s) = \frac{A_0}{1 + s\tau a} \quad (3)$$

Where A_0 is the low-frequency gain of the OA. The gainband product of the OA is defined by:

$$B = \frac{A_0}{\tau a} \quad (4)$$

It is assumed that B^{-1} is much lower than all other time constants in the circuit and the cutoff pulsation is

$$\omega_o = \frac{1}{\tau a} \quad (5)$$

The transimpedance function obtained by straightforward analysis, can be written as

$$\frac{V_s}{R_f \cdot i_d} = \frac{\frac{-A_0}{(1+A_0)} \frac{\omega_o(1+A_0)}{(C_d+C_f)R_f}}{s^2 + s \frac{1+\omega_o(C_d+(1+A_0)C_f)R_f}{(C_d+C_f)R_f} + \frac{\omega_o(1+A_0)}{(C_d+C_f)R_f}} \quad (6)$$

by simplifying the writing of this result, we obtain:

$$\frac{V_s}{i_d} = -R_f \frac{\omega_n^2}{s^2 + s \frac{\omega_n}{Q} + \omega_n^2} \quad (7)$$

with

$$\tau_i = \frac{R_f}{A_0} (C_d + C_f) \quad (8)$$

$$\omega_n^2 = \frac{1}{\tau_i \tau_a} \quad (9)$$

$$\omega_n = 2\pi f_n \quad (10)$$

$$tr = \frac{0.35}{f_n} \quad (11)$$

$$Q = \frac{1}{1 + \eta} \sqrt{\frac{\tau_a}{\tau_i}} \quad (12)$$

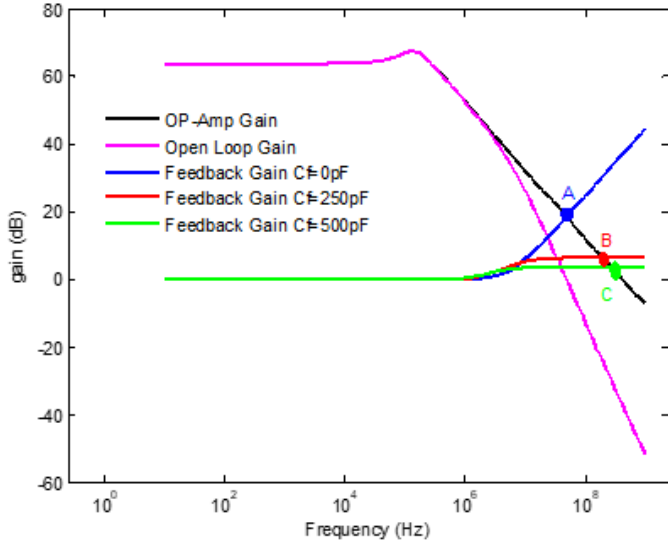


Fig. 8. Gain stability analysis shows that when capacitor C_f has a small value (0pF), the feedback gain transfer slope is 20dB/decade. System is therefore unstable. Increase C_f , feedback gain transfer slope change driving transimpedance towards stability.

$$\eta = \frac{C_f \cdot A_0}{C_d} \quad (13)$$

When detector is represented by its current source and detector capacitance, amplifier will never be used without an appropriate feedback loop. System stability analysis (see Fig. 8 and Fig. 9) [25] shows that when capacitor C_f has a small value ($C_f=0\text{pF}$), the slope of the feedback gain transfer function (20dB / decade) has an opposite value to the OP-Amp gain transfer function (-20dB / decade). Then the system is unstable. An analysis on the phase margin (Fig. 9) shows that it is equal to ($\psi_A = 3^\circ < 45^\circ$) (see point A on the curve). To eliminate this instability, C_f value can be increased.

Fig. 8 & Fig. 9 respectively show that with $C_f=250\text{pF}$, the slope of the feedback gain transfer function is different to (20dB / decade) and phase margin $\psi_B = 74^\circ$ (see point B).

For $C_f= 500\text{pF}$ phase margin $\psi_C = 69^\circ$ (see point C) then the system is stable in these case [26].

Increase C_f will increase envelope delay which is equivalent to individual phase shift $\phi_k(\omega)$ of each pole $S_k = \sigma_k \pm j\omega_k$

$$\phi(\omega) = \arctan \frac{\Im(f(s))}{\Re(f(s))} \quad (14)$$

and the sum of this phase is:

$$\sum_{k=1}^n \phi_k(\omega) = \sum_{k=1}^n \arctan \frac{\omega \pm \omega_k}{\sigma_k} \quad (15)$$

$\tau_e = \frac{d\phi(\omega)}{d\omega}$ who is near to the system feedback time constant $\tau_e \approx R_f \times C_f$.

2) *Input impedance frequency performance*: The system input impedance was investigated.

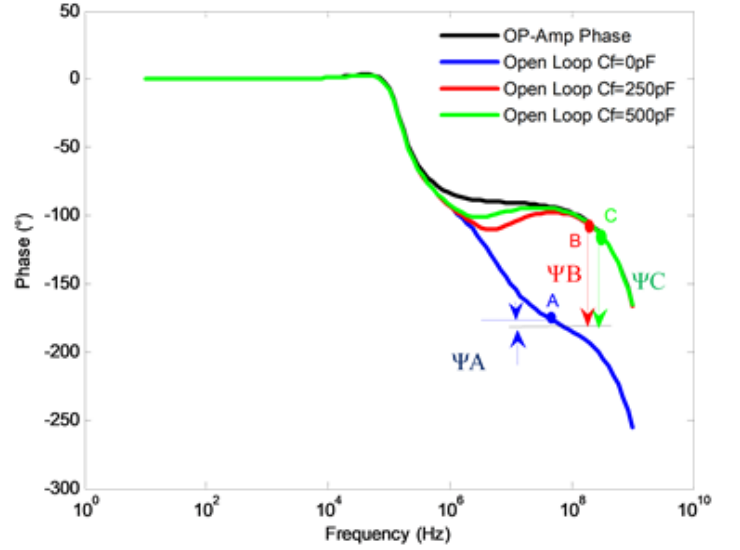


Fig. 9. Phase stability analysis shows that when capacitor C_f has a small value (0pF), open loop phase margin is ($\psi_A = 3^\circ < 45^\circ$)., System is therefore unstable. Increase C_f , open loop phase margin increase driving transimpedance towards stability.

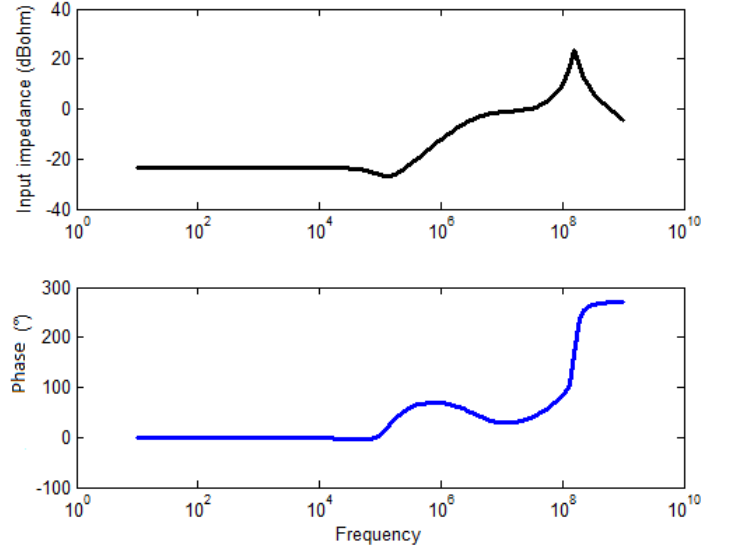


Fig. 10. Input impedance: For low frequency, transimpedance input impedance has a constant value Z_{i1} . This one is proportional to feedback resistance R_f . when frequency increase we observe the effect of Z_{i2} & Z_{i3} which have a pass band & low pass behavior respectively.

$$Z_i = \frac{V_N}{i_d} = \frac{-V_0}{A(s) \cdot i_d} \quad (16)$$

$$i_d = i_c + i_f \quad (17)$$

$$i_d = \frac{V_N}{C_d} + \frac{V_N - V_0}{\frac{1}{R_f} + sC_f} \quad (18)$$

$$R_f \times i_d = -\frac{V_0[sC_d R_f + (1 + A(s))(1 + sC_f R_f)]}{A(s)} \quad (19)$$

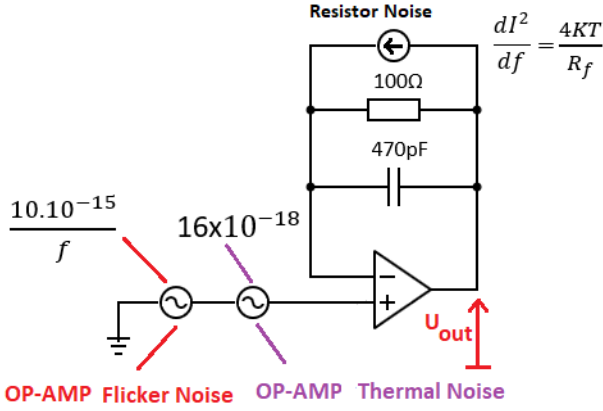


Fig. 11. Simplified Noise model Analysis

$$Z_i = \frac{R_f}{sC_d R_f + (1 + A(s))(1 + sC_f R_f)} \quad (20)$$

$$Z_i = \frac{\frac{R_f}{1+A_0} \frac{(s+\omega_0)(1+A_0)}{(C_d+C_f)R_f}}{s^2 + s \frac{1+\omega_0[C_d+(1+A_0)C_f]R_f}{(C_d+C_f)R_f} + \frac{\omega_0(1+A_0)}{(C_d+C_f)R_f}} \quad (21)$$

As the equation (21) shows, input impedance has three terms ($Z_i=Z_{i1}(Z_{i2}+Z_{i3})$) :

- Frequency independant component:

$$Z_{i1} = \frac{R_f}{(1 + A_0)} \quad (22)$$

- Band pass frequency component:

$$Z_{i2} = \frac{\frac{s(1+A_0)}{(C_d+C_f)R_f}}{s^2 + s \frac{1+\omega_0[C_d+(1+A_0)C_f]R_f}{(C_d+C_f)R_f} + \frac{\omega_0(1+A_0)}{(C_d+C_f)R_f}} \quad (23)$$

- Low pass frequency component:

$$Z_{i3} = \frac{\frac{\omega_0(1+A_0)}{(C_d+C_f)R_f}}{s^2 + s \frac{1+\omega_0[C_d+(1+A_0)C_f]R_f}{(C_d+C_f)R_f} + \frac{\omega_0(1+A_0)}{(C_d+C_f)R_f}} \quad (24)$$

Equation (22) is frequency independant. In first approximation, this equation can be used to evaluate input impedance. Then, in our case $R_f=100$; $A_0=63\text{dB}$; $Z_{i1} = 0.07\Omega$ equal to $-23.36\text{dB}\Omega$ which is a relatively low value (short-circuit) to allow detector charge evacuation towards the preamplifier and not towards detector capacitance Cd [27]. Fig.10 show the curve of the input impedance.

3) *Noise Analysis*: Fig.11 present the model used to characterize the noise [28]. Power density square root of the flicker noise is obtained by locking at $f=1\text{Hz}$ on ADA4817 curve input noise voltage[29]. It is define by:

$$V_{inoise,1/f}(f) = \sqrt{\frac{FNN}{f}} = \frac{100\text{nV}}{\sqrt{Hz}} \quad (25)$$

$$- FNN=(100\text{nV})^2=10 \times 10^{-15} \text{ V}^2$$

- Power spectral density of thermal noise (PSD,Vth) is defined by:

$$\text{PSD,Vth}=(4 \times 10^{-9})^2 = 16 \times 10^{-18} \text{ V}^2/\text{Hz}$$

$$V_{onoise}^2(f) = \left(\frac{10 \times 10^{-15}}{f}\right) + (16 \times 10^{-18}) + \left(\frac{4KT}{R_f} \cdot \left|\frac{R_f \times 1/jC_f w}{R_f + 1/jC_f w}\right|^2\right) \quad (26)$$

The last term can be simplified as

$$\left|\frac{R_f \times 1/jC_f w}{R_f + 1/jC_f w}\right|^2 = \frac{4KTR_f}{(1 + 2\pi f R_f C_f)^2} = \frac{KT}{C_f} \quad (27)$$

$$V_{onoise,RMS} = ((7)^2 \cdot FNN) + (\text{PSD,Vth} \times f_{3dB} \times \frac{\pi}{2}) + \left(\frac{KT}{C_f}\right) \quad (28)$$

$$\text{with } f_{3dB} = \frac{1}{2\pi R_f C_f} = 3.4\text{MHz}$$

$$V_{onoise,RMS} = (49 \times 10 \times 10^{-15}) + (16 \times 10^{-18} \cdot \frac{\pi}{2} \times 3.4\text{MHz}) + (7.85 \times 10^{-12}) \quad (29)$$

The op-amp's thermal noise dominates the output RMS noise. Then :

$$V_{onoise,RMS} = \sqrt{(0.7)^2 + (9.24)^2 + (2.8)^2}$$

$$V_{onoise,RMS} = 9.68\mu\text{V}$$

Output signal is defined by $V_0 = R_f \times i_{fpp}$, then SNR correspond to 0dB is defined by:

$$i_{fpp} = \frac{V_{onoise,RMS}}{100} = \frac{9.68 \times 10^{-6}}{100} = 96.8\text{nA} \quad (30)$$

To have an output signal, input signal should be larger than $i_f > 6 \times i_{fpp}$ which correspond to $0.580\mu\text{A}$.

The following section presents the method used for CSA sizing.

D. Charge Sensitive Amplifier function

The detector charge pulse is transformed into voltage thanks to charge sensitive amplifier (CSA) depicted in Fig.12. If C_f capacitance is very low ($<1\text{pF}$), this circuit will present derivatives or incomplete charge collection. It is for this reason that amplifier's feedback loop must be stabilized by a suitably chosen phase margin, and then capacitance Cf which is linked to system sensitivity [30].

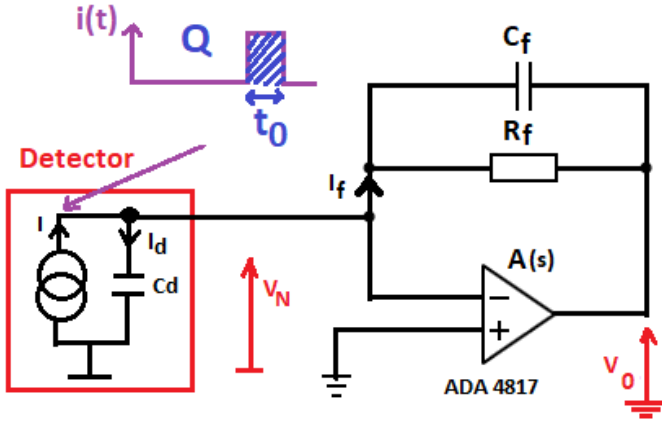


Fig. 12. Charge sensitive Amplifier built around an inverting amplifier.

1) *Charge Sensitive Amplifier analysis:* The amplifier's (OA) voltage gain is modeled in Laplace space as [31]

$$A(s) = \frac{A_0}{1 + s\tau a} \quad (31)$$

Where A_0 is the low-frequency gain of the OA. The gain bandwidth product of the OA is :

$$B = 2\pi \cdot \frac{A_0}{\tau a} \quad (32)$$

It is assumed that B^{-1} is much lower than all other time constants in the circuit and the cutoff pulsation is :

$$\omega_o = \frac{1}{\tau a} \quad (33)$$

The amplifier is designed to measure a charge with a voltage output signal, where the peak amplitude is proportional to the charge at the input. The relation of the output voltage V_0 to the input charge Q is the charge-to-voltage.

$$F_Q = \frac{V_0}{Q} \quad (34)$$

$$i = i_d + i_f \quad (35)$$

With $R_f \approx M\Omega$, $i_R \approx 0$

Expression of the feedback current and detector current is:

$$i_F = \frac{V_0 - V_N}{Z_f} \quad (36)$$

$$i_D = \frac{V_N}{Z_d} \quad (37)$$

The voltage $V_N = \frac{-V_0}{A}$ current-to-voltage transfer function

$$\frac{-V_0}{i} = \frac{A \cdot Z_d \cdot Z_f}{Z_d(A+1) + Z_f} \quad (38)$$

Current is charge derivative $i = \frac{dQ}{dt}$

The corresponding Laplace transformation is

$$\mathcal{L}(Q'(t)) = sQ(s) = i(s) \quad (39)$$

$$Q(s) = \frac{i(s)}{s} \quad (40)$$

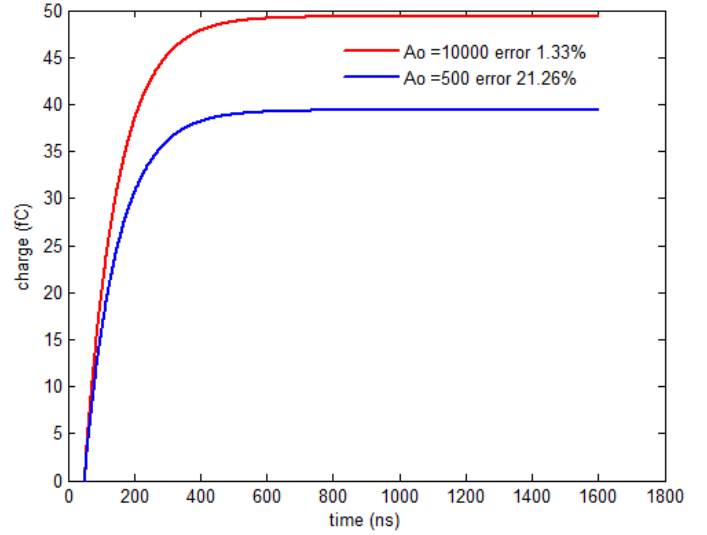


Fig. 13. Influence of finite Gain when 50fC is applied in the input, $C_d=270$ pF, $C_f=2$ pF for 100ns rise time.

If we replace i in the current-to-voltage transfer function from equation (39) by equation (40) and set the feedback impedance, $Z_F = \frac{1}{sC_f}$ and detector impedance $Z_D = \frac{1}{sC_d}$ then the charge to voltage transfer function is given by

$$F_Q = \frac{-A}{C_d + C_f(1 + A)} \quad (41)$$

The open-loop voltage gain of an operational amplifier is frequency dependent, a charge-to-voltage transfer function is obtained by

$$F_Q(s) = \frac{-A_0}{C_d + C_f(A_0 + 1) + s\tau a(C_d + C_f)} \quad (42)$$

$$F_Q(s) = \frac{\frac{A_0}{C_d + C_f(1 + A_0)}}{1 + s \frac{\tau a(C_d + C_f)}{C_d + C_f(A_0 + 1)}} \quad (43)$$

$$F_Q(s) = \frac{-1}{C_f} \times \frac{1}{1 + \frac{C_d}{A_0 \cdot C_f}} \times \frac{1}{1 + s \frac{C_d}{2\pi \cdot GBP \cdot C_f}} \quad (44)$$

The zero-frequency gain is:

$$F_{DC} = \frac{A_0}{C_d + C_f(A_0 + 1)} \quad (45)$$

This result shows that a finite open-loop gain A_o attenuates the measured peak voltage. If A_o has a high value, output signal will be independent of the value of detector capacitance (Fig. 13).

Another parameter of the CSA is output voltage rise time measured by applying charge step at its input.

$$\left| \frac{F_Q(j2\pi \cdot f_c)}{F_Q(0)} \right| = \frac{1}{\sqrt{2}} \quad (46)$$

$$f_c = B \frac{\frac{C_d}{C_f} + (A_0 + 1)}{A_0 \left(\frac{C_d}{C_f} + 1 \right)} \quad (47)$$

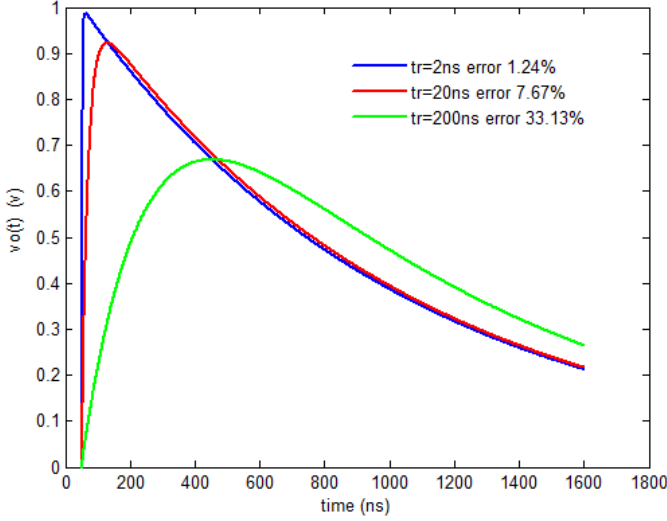


Fig. 14. CSA rise time (τ_r) influence on ballistic deficit. Fast CSA lead to reduce ballistic deficit. This plot is done with $\tau_f = R_f * C_f = 1\mu\text{S}$; and $C_d = 270\text{pF}$

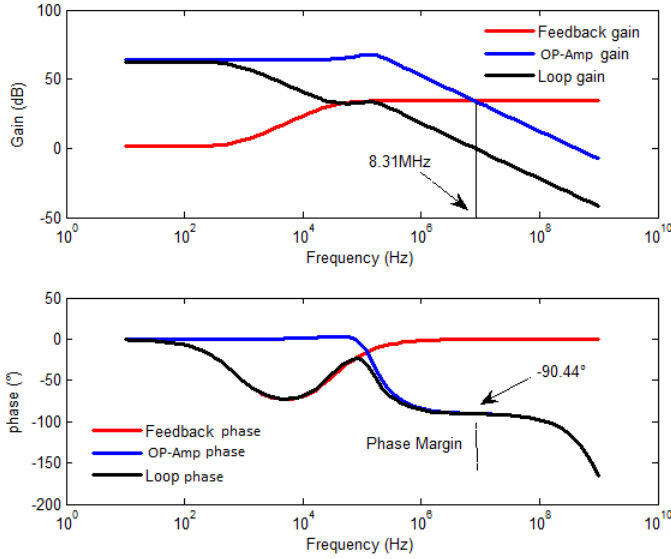


Fig. 15. Gain and Phase stability analysis. The phase margin at $F = 8.3\text{MHz}$ is roughly 89.76° . System is therefore stable.

$$\lim_{A_0 \rightarrow \infty} f_c = \frac{B}{\frac{C_d}{C_f} + 1} \quad (48)$$

This result shows that the cutoff frequency and therefore the rise time of the CSA, are inversely proportional to the gain-bandwidth product of the amplifier [32].

$$\tau_r = 2.2 \cdot \frac{C_d}{2 \cdot \pi \cdot B \cdot C_f} \quad (49)$$

The unit step response showing rise time influence is presented in Fig. 14.

To reduce the rise time we have chosen a high speed low noise OP-amp ADA4817 (1GHz). Because charged particle beam energy is very high we have chosen $C_f = 5.3\text{pF}$ to make sure that the electronics will not saturate. Then, stability has

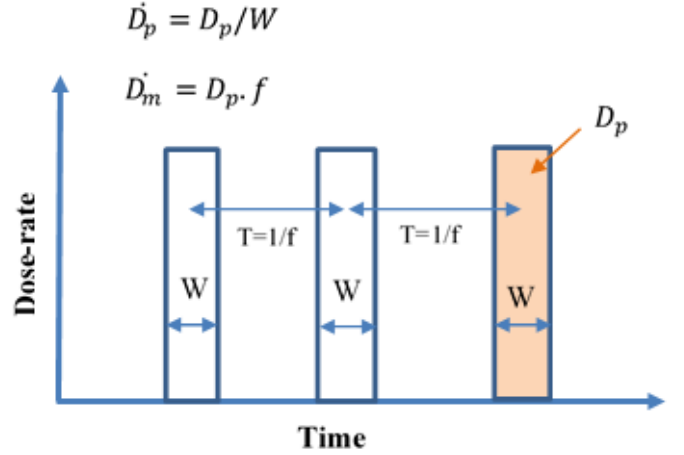


Fig. 16. Temporal structure of an ideal rectangular pulsed beam: dose-rate as a function of time. f is the pulse repetition frequency, w the temporal pulse width and D_p the dose-per-pulse. D_m and \dot{D}_p are the mean dose-rate of the beam and the mean dose-rate in the pulse, respectively.

been studied [33]. The transfer function Bode plot (open loop gain (Aol), Feedback gain β and the loop gain Aol). β plot shows that at $F = 8.3\text{MHz}$ the phase margin is roughly $89.76^\circ > 45^\circ (180^\circ - 90.24^\circ = 89.76^\circ)$. This is sufficient for a stable operation (see Fig. 15).

IV. MATERIAL, TEST METHOD AND MEASUREMENT RESULTS

A. Material

The machine used is a high dose-per-pulse prototype linear accelerator (linac) delivering high energy pulsed charged particle beam. This machine is able to reach a higher beam current. This machine offers the possibility to vary the dose-per-pulse and dose-rate over a large range (Fig. 16). This machine is not equipped with semi-transparent monitor chamber to control the beam as usually found because of the saturation [34] due to the high dose of charged particle. However, beam signals are recorded from a current transformer measuring the beam current at exit window of the accelerating section and from the primary collimator signal (Fig. 17).

1) *Dose variation approaches* : RHF (Reflected High Frequency) power change with power supplied (*Ugrid*): The simplest means of varying the linac's output dose is to change the RHF power supplied of accelerator and hence change the field strength in the accelerating cavities [35].

Width (W): The linac's output dose can change by varying the pulsed beam width [36].

Frequency (F): The linac's output dose can change by varying the frequency of the signal [37].

B. Test Methode: Experimental Result

1) *PAI Experimental result*: Front-End Amplifier has been implemented as shown in Fig. 18 using ADA4817 OP-amp

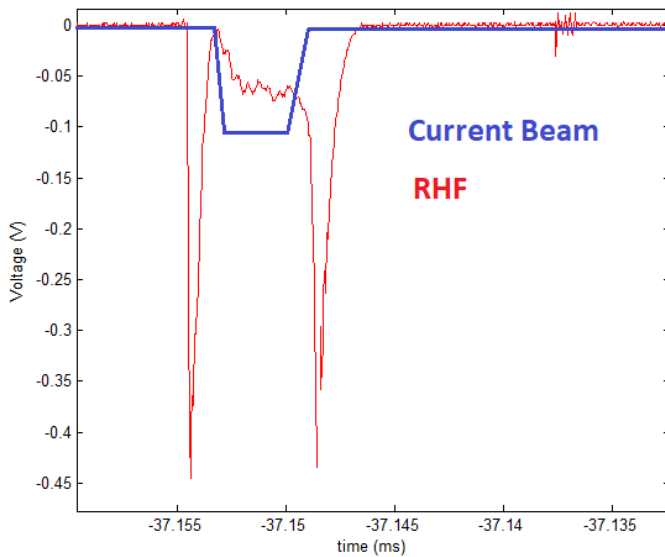


Fig. 17. Current transformer measuring the beam current. Red color is RHF and Blue color is current transformer measuring during canon opening.

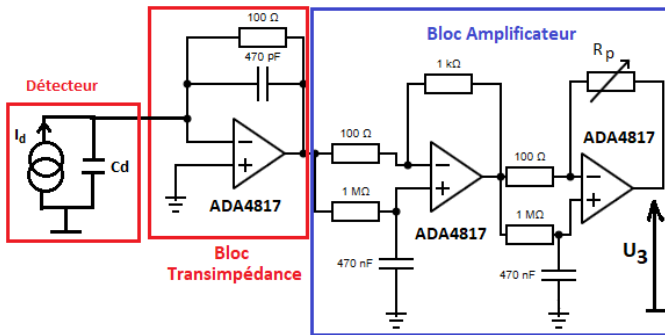


Fig. 18. Electronic Front-End built around transimpedance amplifier with two amplifiers stages.

with $R_f=100\Omega$ and $C_f=470\text{pF}$ in order to obtain a peaking time below 200ns and maximize the signal to noise ratio. Transimpedance amplifier was performed for the complete circuit including two amplifier circuit to amplify the detector signal to 92.84db Ω . The supply OP-amp voltage is $\pm 5\text{V}$.

The complete circuit is simulated considering that the input signal has $I_{\text{pulse}}=20\mu\text{A}$, and that $C_d=270\text{pF}$ the peaking time and amplitude of the output are 167ns and 178.44mV respectively. The shape of the input current and the output voltage pulse obtained by simulation are shown in Fig.19.

Emulator (Fig. 20) was tested with an input pulse voltage source in series with his 50Ω input resistance, the signal is carried with 50Ω cable [38]. To adapt the impedance, we should place another 50Ω resistance and then convert voltage pulse to current pulse with $10\text{k}\Omega$ resistance. Capacitor of 270 pF is placed in parallel with the TIA input to emulate the SiC detector capacitance. The experimental result is presented in Fig. 21.

2) *CSA Experimental result*: Complete circuit amplifier has been implemented as shown in Fig. 22 using ADA4817 OP-

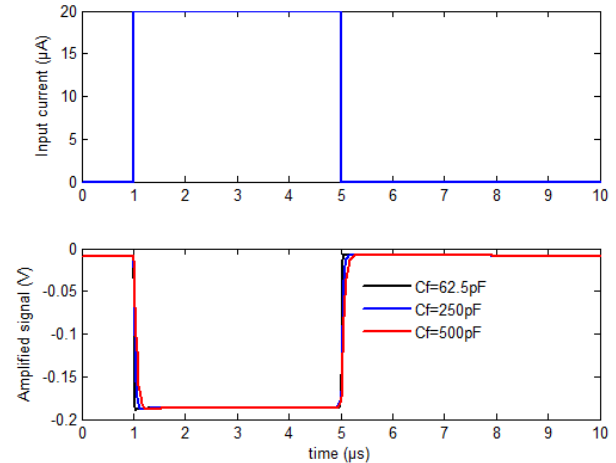


Fig. 19. Simulation result with input current form which represents detector output current.

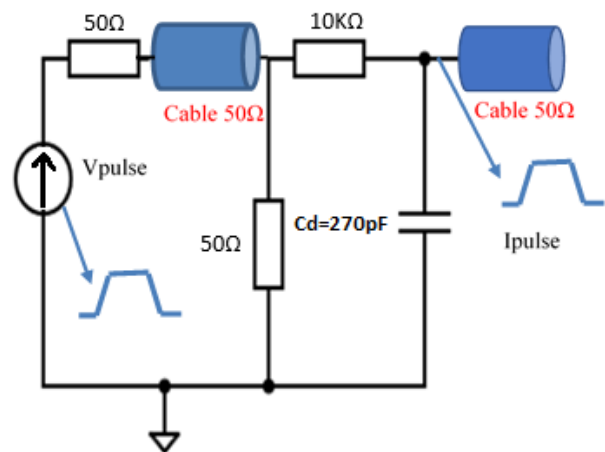


Fig. 20. Emulator schematic used for current experimental test.

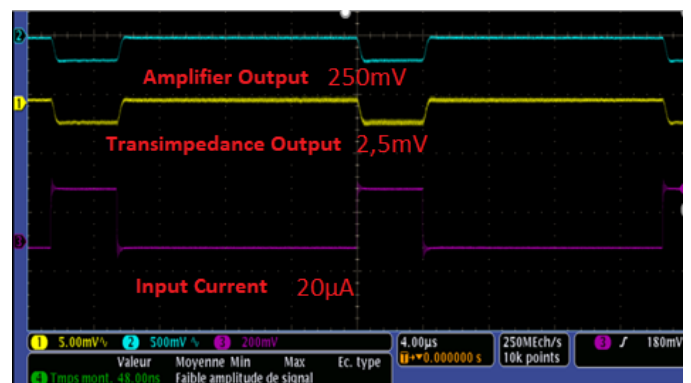


Fig. 21. System response to emulator. input $20\mu\text{A}$ is applied, transimpedance output has 2.5mV voltage peak, amplified signal has 250mV voltage peak.

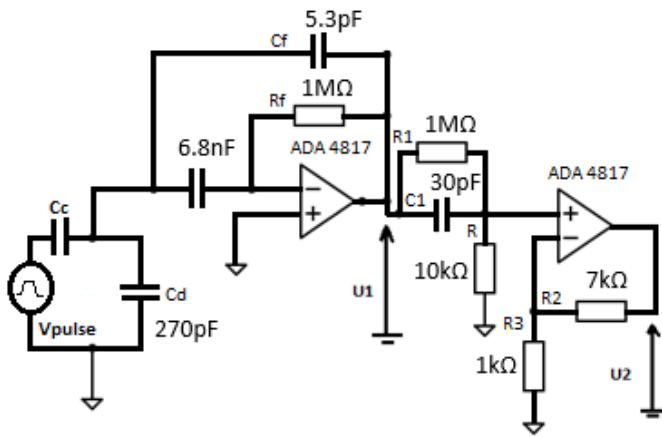


Fig. 22. Charge sensitive amplifier built around inverter amplifier and pole zero cancellation.

amp with $R_f=1\text{M}\Omega$ and $C_f=5.3\text{pF}$ in order to reduce rise time and maximize the signal to noise ratio. Charge sensitive amplifier was performed for the complete circuit including one stage of pole zero cancellation circuit to improve peak shapes and energy resolution [39]. The system transfer function is defined by:

$$\frac{U_2}{Q_o} = \frac{1}{C_f} \cdot \frac{R_2}{R_3} \cdot \left(\frac{1}{s + \left(\frac{R+R_1}{R_1 \cdot R} \right) \frac{1}{C_1}} \right) \quad (50)$$

In simulation domain

$$Q_o = V_{pulse} \times C_c \quad (51)$$

In radiation test

$$Q_o = \frac{E \cdot e}{\epsilon} \quad (52)$$

Where E is the absorbed energy within the detector active volume, ϵ is the energy required to create an electron-hole pair which is 7.78 eV in SiC and e the electron charge.

This circuit has been designed to measure the detector charges level when traditional detector used saturates .

The complete circuit is simulated (with $1\text{G}\Omega$ resistance placed in parallel with C_d to allow OP-AMP polarization) considering that the current time duration is 200ns with the following relation:

$$i = \frac{du(t)}{dt} \quad (53)$$

$C_d=270\text{pF}$, input charge $Q=400\text{fC}$.The shape of the input voltage and the output voltage(U_1 and U_2) pulse obtained by simulation are shown in Fig.23.

The circuit was tested with an input pulse voltage source [40] in series with his 50Ω input resistance, The signal is carried with 50Ω cable. To adapt the impedance we should place another 50Ω resistance and then convert voltage pulse to charge with 2pF capacitor. 270pF detector capacitor is then placed in parallel with the CSA input to emulate the SiC detector capacitance (Fig.24). The experimental result is presented in Fig. 25.

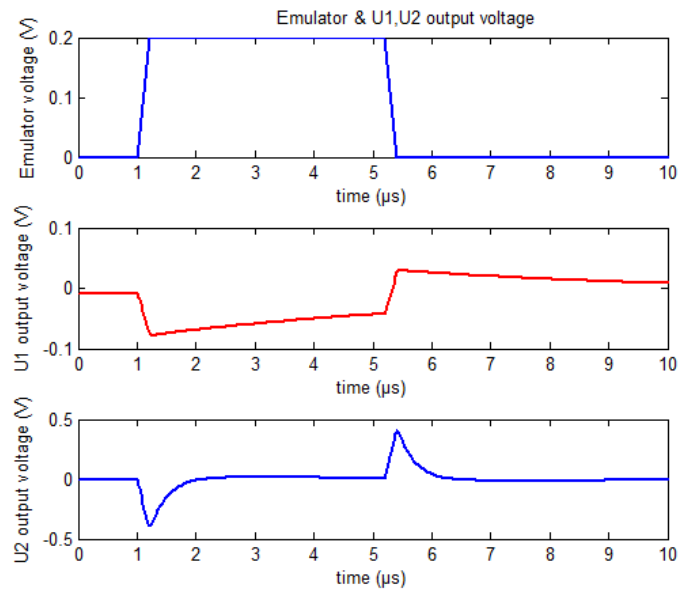


Fig. 23. Simulation result with input voltage who has 200ns rise time and fall time respectively, 270pF detector capacitance in parallel.

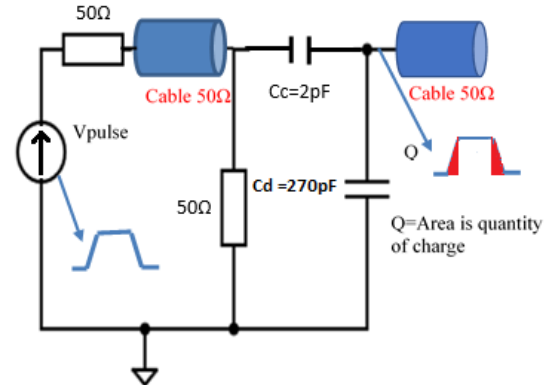


Fig. 24. Emulator schematic used for charge experimental test.



Fig. 25. Experimental result with 80fC input charge applied which correspond to $U_1=200\text{mV}$. AFE response voltage is $U_2=20\text{mV}$.

Measured	Frequency (Hz)	Number of pulses	Time (ms)	Width (μ s)	Grid voltage (V)	Detector Voltage Bias (V)
T1	100	20	200	4	140	0
T2	100	20	200	4	180	0
T3	100	20	200	4	220	0
T4	100	20	200	4	260	0
T5	100	20	200	2	300	0
T6	100	20	200	0.8	300	0

TABLE III
BEAM PARAMETER USED IN PAI MODE.

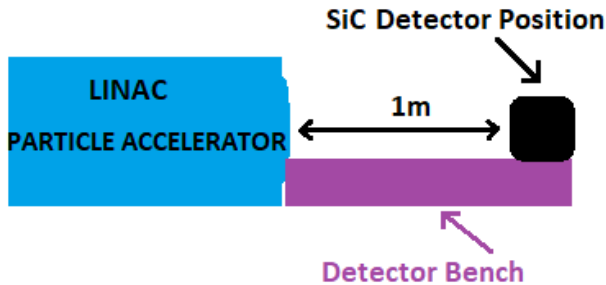


Fig. 26. Setup for SiC detector used in high dose per pulse charged particle beam.

C. Measurement results

1) *PAI System of test:* The system (detector and electronic) has been tested with high dose per pulse Linac. Their machine produce high charged particle beam Irradiation. Tests parameters are presented in Tab.III. We studied the front end electronic performance with defined configuration Fig.26, first of all by analysing the output signal shape when we are in T1(Tab.III) configuration, electronic do not saturate. We can observe it thanks to the temporal and amplitude occupation.

Fig. 27 show Reflected High Frequency (RHF) displayed as voltage vs. time plots. Values for the beam and the gun current are obtained with the conversion $1 \text{ V} = -1 \text{ A}$, while a correction factor of -50 is applied for the collimator and the reflected high frequency since their output are connected

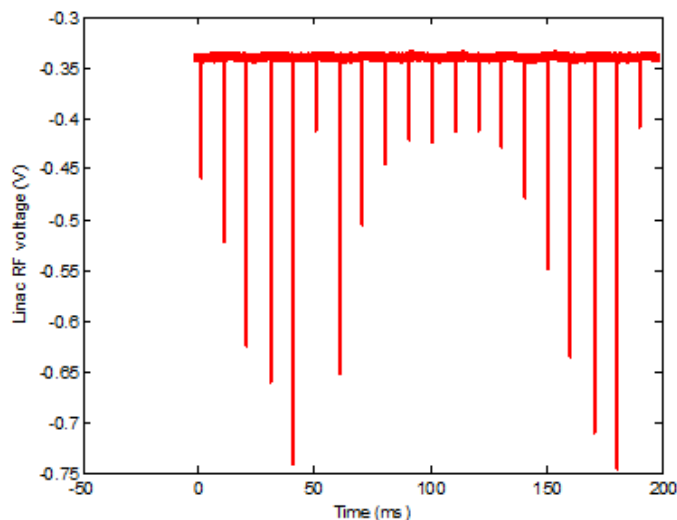


Fig. 27. Linac RHF Voltage with the conversion $1 \text{ V} = -1 \text{ A}$.

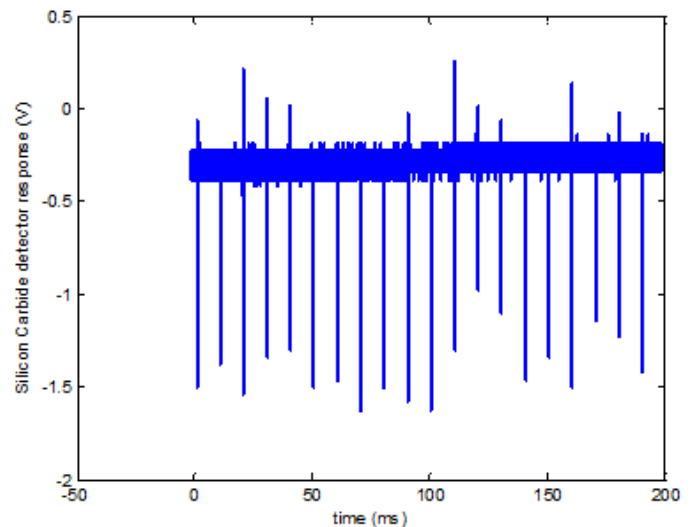


Fig. 28. Electronic Front-End result to measure the average detector output current.

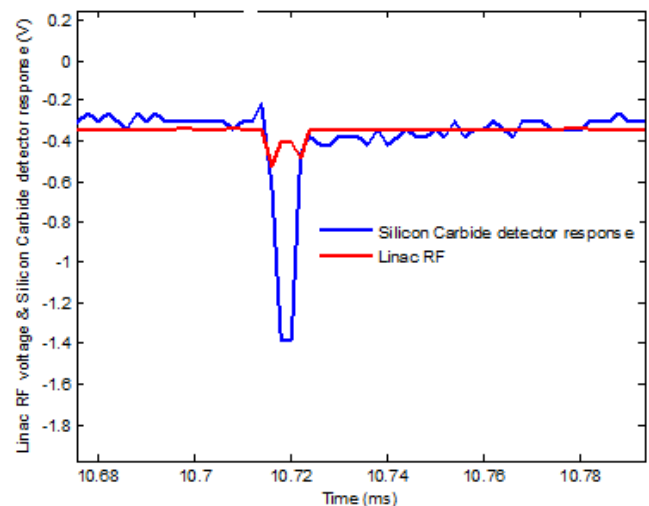


Fig. 29. Electronic response and RHF(Reflected high frequency) displayed as voltage vs time for T1 (TABLE III).

to a 50Ω resistance. Fig.28 is electronic front end output displayed as voltage vs time plots and Fig.29 zoom on a peak hold on between RHF signal and electronic front end output. Signal is applied during 200ms with 100HZ frequency for a total of 20 pulse, and $4\mu\text{s}$ width. The shape of the signal generated by electronic front end has the same form as that of the signal generated by the intensity transformer (Fig. 17).

2) *CSA System of test:* Tests parameters is presented in Tab.IV. We studied the front end electronic performance with defined configuration Fig.26. First of all by analysing the output signal shape when we are in T1(Tab.IV) configuration, electronic do not saturate.

We can observe it thanks to the temporal and amplitude occupation Fig.30 shows reflected high frequency (RHF) displayed as voltage vs time. Values for the beam and the gun current are obtained with the conversion $1 \text{ V} = -1 \text{ A}$, while a correction factor of -50 is applied for the collimator and the

Measure	Frequency (Hz)	Number of pulses	Time (ms)	Width (ns)	Grid voltage (V)	Detector Bias (V)
T1	100	20	200	200	300	0
T2	100	20	200	200	200	0
T3	100	20	200	200	150	0
T4	100	20	200	200	160	0
T5	100	20	200	200	120	0

TABLE IV
BEAM PARAMETER IN CSA MODE.

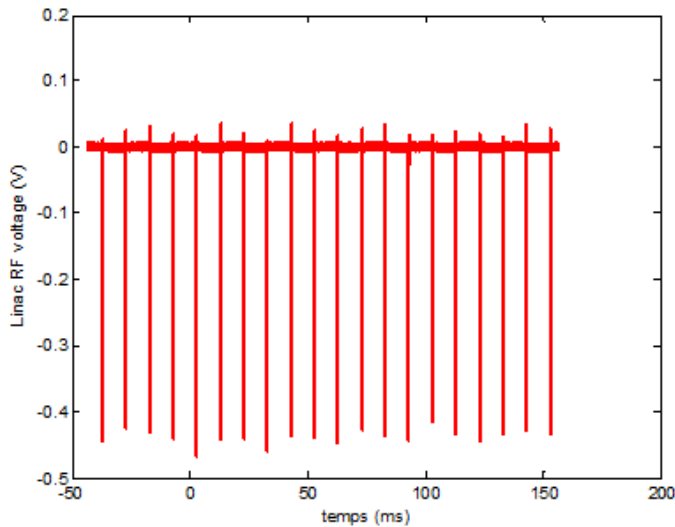


Fig. 30. Linac Rf Voltage with the conversion $1V = -1A$.

reflected high frequency since their output are connected to a 50Ω resistance. Fig.31 is electronic front end output displayed as voltage vs time for configuration in T1(Tab.IV) mesure. Fig.32 is a zoom on a peak hold on between RHF signal and electronic front end output. We observed that the signal is surrounded by noise. Signal is applied durind 200ms with 100HZ frequency for a total of 20 pulse and 200ns pulse width. Signal shape generated by electronic front end during the collection time (200ns), has the same form as the integral

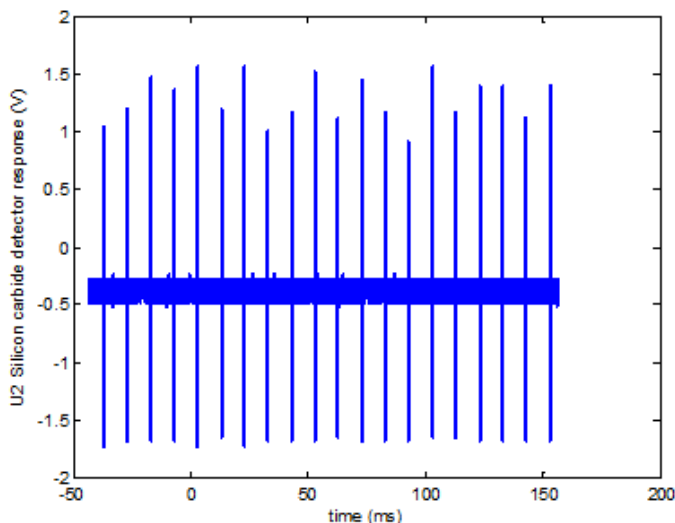


Fig. 31. Electronic Front-End result to measure the collected charges which represents the current integral generated by the detector.

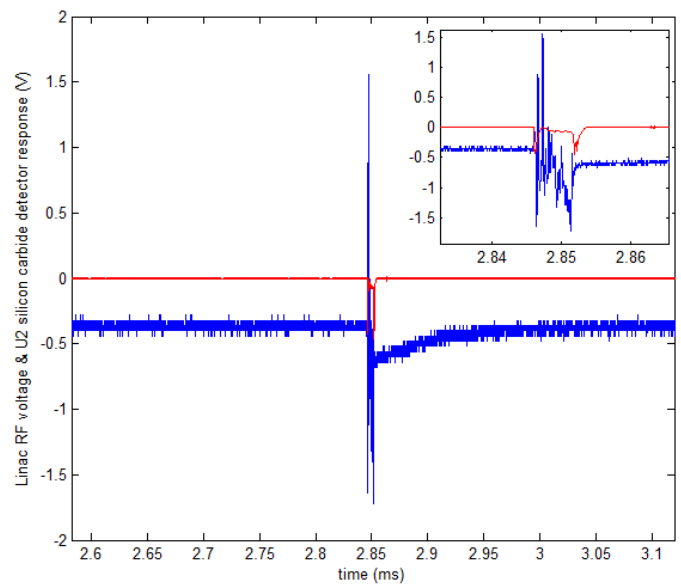


Fig. 32. Electronic response and RHF(Reflected high frequency) displayed as voltage vs time for T1 (Tab.IV) configuration.

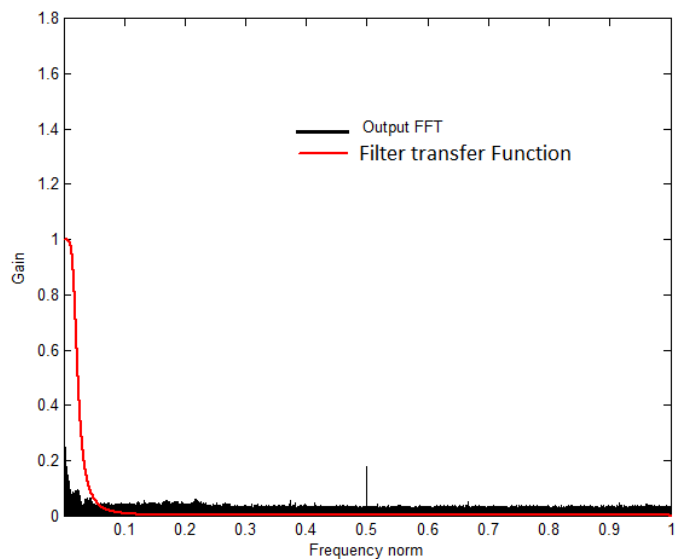


Fig. 33. Output fast fourier transform (black color) and butterworth filter transfert function used (red color) to remove noise.

of the signal generated by the intensity transformer Fig. 17.

Mathematical model which allows us to eliminate the noise surrounding the signal is low pass filter (Fig.33). We use butterworth filter with with 0.02 as normalized frequency . This technique smoot out high frequency fluctuations. By applying this filter to the signal, we have a response in Fig.34. This result allows us to appreciate the charge collection time which is directly related to the time domain signal delivered by the RHF.

D. CSA Linearity curve

In order to link the output variations to the input charge, a simple relationship is necessary. Then the linearity of the

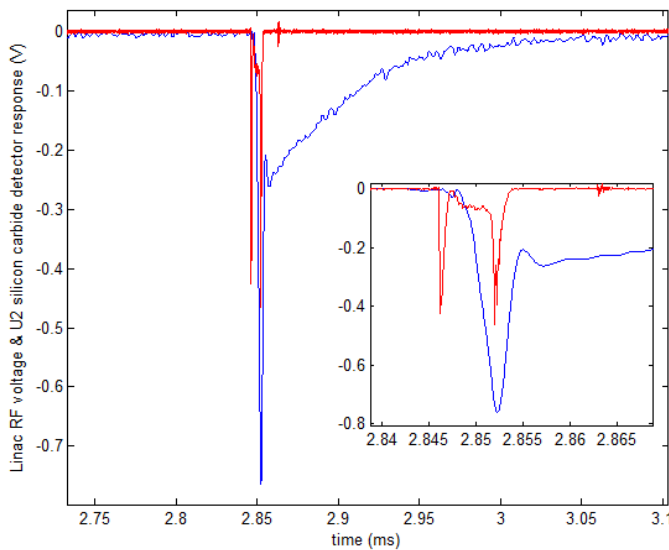


Fig. 34. Front-End output signal after applying low pass filter. Charged particle current beams is applying during 200ns see T1 in Tab.IV

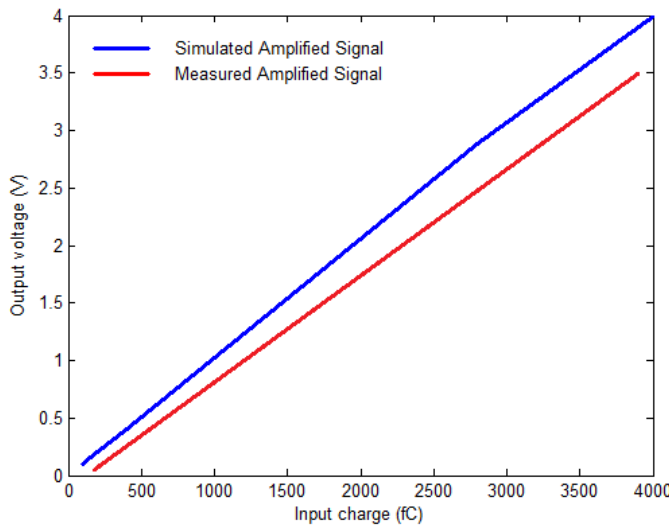


Fig. 35. Linearity curve of the Charge sensitive amplifier and zero pole cancellation see Fig.22.

system response has been checked Fig.35.

E. PAI Linearity curve

In order to link the output variations to the input currents, a simple relationship is necessary. Then the linearity of the system response has been checked Fig.36.

V. DISCUSSION AND CONCLUSION

In beams of higher intensity, it is impossible to count the pulses separately. The reasons are multiple but in this work we focused on two main causes. first of all in beams of higher intensity, all online detector (ion-chambers, silicon diodes, GaAs) saturates (ions collection efficiency decrease).

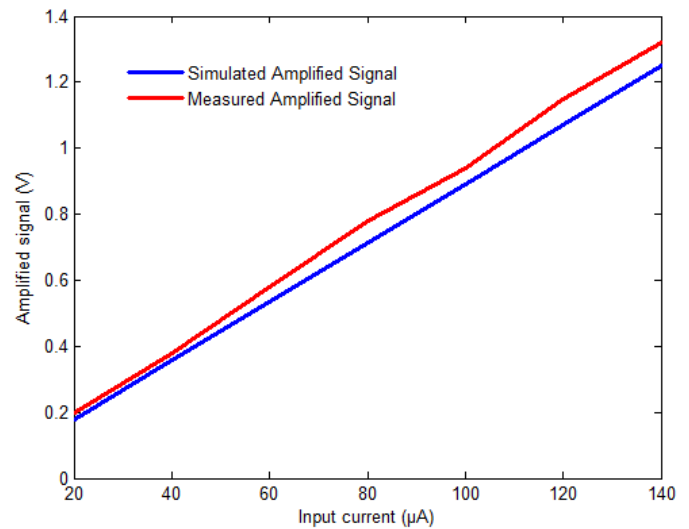


Fig. 36. Linearity curve of current amplifier Front-End see Fig.18.

Secondly, the response time of the front-end can also be the cause.

So, Silicon carbide detector with high capacitance (270pf) has been developed by the laboratory for harsh environment applications. With this electronic we have recovered signal detector emitted with low rise time ($< 200\text{ns}$) in PAI mode for high detector capacitance and also in CSA mode. As we have shown in the previous sections, we have succeeded to count separately the pulses. The rest of the work will consist to connect this Front-End to a processing system. In the near future, we will develop a high speed front end to reduce rise time below 30ns and next design an integrated electronic circuit. This reconfigurable front-end electronic will be able to extract all useful signals (current or charge answer) from the detector having Different characteristics (high and low capacity) and resolved data (nature of the particle, spectroscopy, etc.) will be done with on-board processor. Our system will take into account the environment of use.

REFERENCES

- [1] Lebedev, A.A. & Kozlovski, V. & Strokan, Nikita & Davydov, D. & Ivanov, Alexander & Strel'chuk, Anatoly & Yakimova, Rositsa. (2003). Radiation Hardness of Silicon Carbide. Materials Science Forum - MATER SCI FORUM. 433-436. 957-960. [10.4028/www.scientific.net/MSF.433-436.957](https://doi.org/10.4028/www.scientific.net/MSF.433-436.957).
- [2] Hrubčín, L., Gurov, Y.B., Zaiko, B. et al. A Study of the Radiation Hardness of Si and SiC Detectors Using a Xe Ion Beam. Instrum Exp Tech 61, 769-771 (2018). <https://doi.org/10.1134/S0020441218060192>.
- [3] G. Bertuccio, D. Puglise, D Macera, R. Di Liberto, M. Lamborizio, L. Mantovani "Silicon Carbide Detectors for in vivo Dosimetry", IEEE Trans. On Nucl. Sc., pp.2-04, 2014.
- [4] B. L. Gregory and C. W. Gwyn, "Radiation effects on semiconductor devices," in Proceedings of the IEEE, vol. 62, no. 9, pp. 1264-1273, Sept. 1974, doi: 10.1109/PROC.1974.9605.
- [5] Krzysztof Iniewski, "Radiation Effects in Semiconductors", vol11, CRC Press, 2010, pp. 3-27.
- [6] Helmuth Spieler. "Semiconductor Detector Systems", Clarendon Press. Oxford 2005, pp. 54-98.
- [7] Robert W. Kuckuck. "semiconductor detector for use in the current mode", pp. 21-45.

- [8] B. Chantepie. "Étude et réalisation d'une électronique rapide à bas bruit pour un détecteur de rayons X à pixels hybrides destiné à l'imagerie du petit animal", Thèse de Doctorat Aix-Marseille II, 2008. pp. 30-45.
- [9] P. Chevallier "Détection et Mesure des Rayonnements Nucleaires", Techniques de l'ingénieur, Vol 1, ref.:P2250, pp.10-04-1996.
- [10] Characteristics and use of charge amplifier.(2017) viewed at https://www.hamamatsu.com/resources/pdf/ssd/charge_amp_kacc9001e.pdf.
- [11] Paul Muller, Yusuf Lebledici. "Cmos Multichannel Single-Chip Receives for MultiGigabit Optical Data Communication", Springer, 2007, pp. 73-93.
- [12] Mohammad Nakhostin, "Signal Processing for Radiation Detectors ", vol.1, Wiley, 2018 , pp. 261-292.
- [13] Eduard Säcker, "The Transimpedance Limit" IEEE Transactions on Circuits and Systems-I-VOL. 57, NO. 8, AUGUST 2010.
- [14] M. d. M. Silva and L. B. Oliveira, "Regulated Common-Gate Transimpedance Amplifier Designed to Operate With a Silicon Photo-Multiplier at the Input," in IEEE Transactions on Circuits and Systems I: Regular Papers, vol. 61, no. 3, pp. 725-735, March 2014, doi: 10.1109/TCSI.2013.2283992.
- [15] Low Noise Amplifiers for Small and Large Area Photodiodes available at https://www.analog.com/media/en/reference_design_documentation/design-notes/dn399f.pdf. Accessed 10 October 2018.
- [16] F Nava1, G Bertuccio, A Cavallini and E Vittone,"Silicon carbide and its use as a radiation detector material ", Measurement Science and Technology, Meas. Sci. Technol. 19, 2008,25p.
- [17] Syed Naeem Ahmed , "Physics and Engineering of Radiation Detection", First edition 2007 , Elsevier , pp. 267-270.
- [18] R.C. Haight,"Fast-neutron detectors for nuclear physics experiments",2nd International workshop on fast neutron detectors and applications, November 6–11 2011.
- [19] F. Issa, L. Ottaviani, D. Szalkai, L. Vermeeren, V. Vervisch, A. Lyoussi, R. Ferone, A. Kuznetsov, M. Lazar, A. Klix, O. Palais, "4H-SiC Neutron Sensors Based on Ion Implanted 10B Neutron Converter Layer": IEEE Transactions on Nuclear Science Vol. 63 (3): 1976-1980 June 2016.
- [20] François DIVOUX,"Détection des neutrons par semi-conducteur dans un coeur de reacteur atomique ",Centre d'Etudes Nucléaires de Grenoble,Rapport CEA - R . 3304,1968,14,21.
- [21] "Comparaison du Diamant et du Carbure de Silicium (SiC) pour la détection de neutrons en milieux nucléaires", Thèse de Doctorat Aix-Marseille, 2018.
- [22] Luis B.Oliveira "Noise Performance of a Regulated Cascode Transimpedance Amplifier for Radiation Detectors ": IEEE Transactions on Circuits and Systems Vol. 59, NO.9, March 2012.
- [23] Transimpedance Amplifier Stability. (2019). consulted at <https://www.allaboutcircuits.com/technical-articles/transimpedance-amplifierstability> fbclid=IwAR3W9Wckwft1BhqAF64T657r3IB5yXIKOROKYpx9NTfPZ6QiXft015UPk.
- [24] Manuel de Medeiros Silva, "Regulated Common-Gate Transimpedance Amplifier Design to Operate with a Silicon Photo-Multiplier at the Input ": IEEE Transactions on Circuits and Systems Vol. 61, NO.3, March 2014.
- [25] Transimpedance Amplifier Stability at <https://www.allaboutcircuits.com/technical-articles/transimpedance-amplifier-stability>.
- [26] John Caldwell, "Op Amp Bandwidth for Transimpedance Amplifier-1", course, Tina-Ti, 2020.
- [27] Erik Margan, "Transimpedance Amplifier Analysis", consulted at http://www-f9.ijs.si/margan/Articles_trans_z_amplifier.pdf.
- [28] R. Jacob Baker, "CMOS Circuit Design, Layout, and Simulation ", Third Edition ,WILEY, pp. 213-262.
- [29] consulted at https://www.analog.com/media/en/technical-documentation/datasheets/ADA48171_48172.pdf.
- [30] Les préamplificateurs dans la chaîne d'instrumentation nucléaire. Seminaire Ganil (2017) consulted at <https://docplayer.fr/82488438-Les-preamplificateurs-dans-la-chaîne-d-instrumentation-nucléaire.html>.
- [31] Sabrina BEN KRIT, "Etude et développement d'une chaîne de traitement analogique du signal dédiée à la détection de particules en environnement sévère", Thèse de doctorat de l'université d'Aix-Marseille, Décembre, 2015.
- [32] Fodisch. P, Berthel. M, Lange. B, Kirschke. T, Enghardt. W, Kaefer. P "Charge Sensitive FrontEnd Electronics with Operational Amplifiers for CdZnTe Detectors", in JINST 11 (2016) T09001, 16 Mar 2016.—mult. p. DOI :10.1088/1748–0221/11/09/T09001.
- [33] A. Giachero, C. Gotti, M. Mainoa, G. Pessina, "Current feedback operational amplifiers as fast charge sensitive preamplifier for photomultiplier readout": Journal of Instrumentation, Volume 6, May 2011.
- [34] Maud Jaccard, Maria Teresa Durán, Kristoffer Petersson, Jean-François Germond, Philippe Liger, Marie-Catherine Vozenin, Jean Bourhis, François Bochud, Claude Bailat,"High dose-per-pulse electron beam dosimetry: Commissioning of the Oriatron eRT6 prototype linear accelerator for preclinical use": Research Article doi: 10.1002/mp.12713.
- [35] L.Marleau. "Introduction à la physique des particules", pp. 36, 2017.
- [36] P. G. Jorge, M. Jaccard, K. Petersson et al, Dosimetric and preparation procedures for irradiating biological models with pulsed electron beam at ultra-high dose-rate, Radiotherapy and Oncology, <https://doi.org/10.1016/j.radonc.2019.05.004>.
- [37] Samy Hanna, Microwave Innovative Accelerators (MINA), Danville, CA 94506, U.S.A, "Review of energy variation approaches in medical accelerators": Proceedings of EPAC08, Genoa, Italy.
- [38] Helmuth Spieler. "Semiconductor Detector Systems", CLARENDON PRESS . OXFORD 2005, pp. 54-98.
- [39] Grybos, Pawel & Szczygiel, Robert. (2008). Pole-Zero Cancellation Circuit With Pulse Pile-Up Tracking System for Low Noise Charge-Sensitive Amplifiers. Nuclear Science, IEEE Transactions on. 55. 583 - 590. 10.1109/TNS.2007.914018.
- [40] Sukhrani, Niharika. R. and Prakash Vaidya. "Simulation of Charge Sensitive Preamplifier using Multisim Software."(2015).



A. Tchoulack. Tchamako is PHD student at Aix Marseille University, IM2NP (UMR 7334), Marseille, France. He is with Integrated Circuit Design department and IRM-PV team (tchoulack12@yahoo.fr). His research activity concerned the development of a reconfigurable Front-End (CMOS 0.35 μm) electronic for particle detection (Neutron, UV and Charged particle). The detector used is silicon carbide. He received the B. Sc. degree in electrical engineering from IUT-FV Bandjoun, Cameroun, in 2009 and the M. Sc in microelectronic from Aix-Marseille University, France, in 2017.



Dr Laurent. Ottaviani is Associate Professor and Senior Lecturer at the Aix-Marseille University (IM2NP / UMR 7334). He is in charge of research programmes related to Silicon Carbide in its applications to optoelectronic and neutron sensor devices. He focused his research in SiC and its use in detectors since his PhD completed in 1999 (INSA Lyon – France). Over these years, he has developed intensive experience in instrumental physics related to neutron detectors, UV photodetectors and solar cells, as well as theoretical and experimental knowledge in SiC doping using ion implantation Technologies. He supervised 9 PhDs, filed 3 patents and has authored or co-authored more than 50 papers published in refereed journals. He is member of Scientific Committee of 5 international conferences, including IEEE NSS – Nuclear Science Symposium and ANIMMA - International Conference on Advancements in Nuclear Instrumentation, Measurement Methods and their Applications. He is member of the international editorial board of Frontiers in Physics - Radiation Detectors and Imaging (laurent.ottaviani@im2np.fr).



Prof. Dr. Wenceslas RAHAJANDRAIBE is currently full professor at the University of Aix-Marseille. He received the B. Sc. degree in electrical engineering from Nice Sophia-Antipolis University, France, in 1996 and the M. Sc. (with distinction) in electrical engineering from the University of Montpellier, Science department, France, in 1998. Since 1998, he joined the microelectronics department of Informatics, Robotics and Microelectronics Laboratory of Montpellier (LIRMM) and received the Ph. D. on Microelectronics from the University of Montpellier. Since 2003, he joined the microelectronic department of Materials, Microelectronics and Nanoscience Laboratory of Provence (IM2NP) in Marseille, France where he was an Associate Professor. Since 2014, he is a Professor at Aix Marseille University where he heads the Integrated Circuit Design group of the IM2NP laboratory. He heads the Integrated Circuit Design group since 2013. He directed and co-supervised 18 PhD and 15 Master students. His research interests involve AMS and RF circuit design from transistor to architectural level. His present research activity is focused on ultralow power circuit design for smart sensor interface and embedded electronic in bioelectronic and e-health applications, wireless systems, design technique and architecture for multi-standard transceiver. He is author or co-author of 8 patents and more than 120 papers published in refereed journals and conferences. He is an expert for the ANR, the French Agency for Research. He has served on program committees of IEEE NEWCAS and ICECS. He has been and is a reviewer of contributions submitted to several IEEE conferences and journals such as ISACS, NEWCAS, MWSCAS, ESSCIRC, ESSDERC, RFIC, IEEE Transactions on Circuits and Systems I and II, IET Electronics Letters. (wenceslas.rahajandraibe@im2np.fr).



Wilfried. Vervisch has been working on semiconductors for almost 20 years. He worked on power devices, energy recovery, solar cells and detection devices. He is a specialist in modelisation and simulation, particularly in Monte Carlo, finite element calculations... Besides, he developed several detection devices until measurements under radiations environment. (wilfried.vervish@im2np.fr).



Vanessa. Vervisch is a PhD from Aix Marseille University. During several years she worked on semiconductor material for solar cells fabrication but since 2012 she is focused on particles detection (fast and thermal neutrons) based on wide band gap semiconductor. (vanessa.vervisch@gmail.com).



Jean-Pierre Walder CNRS research engineer, is currently responsible for the IOLab platform of the IM2NP UMR CNRS 7334 laboratory. This platform brings together the resources for characterizing connected objects and designing mixed integrated circuits. He has nearly thirty years of expertise in the design of complex mixed digital / analog circuits in CMOS and Bipolar technology. He notably joined the Lawrence Berkeley National Laboratory (LBNL) in Berkeley in California for 12 consecutive years by developing numerous circuits for various applications such as medical, space and particle physics. He then joined IM2NP in 2015 for the design of a mixed CMOS integrated circuit, as part of the APPRISE project funded by the AMIDEX foundation for the reading of electrographic signals (EKG). (jean pierre.walder@im2np.fr).